Supporting Information

Oh et al. 10.1073/pnas.0811923106

SI Text

Hysteresis of BPE-PTCDI MW-TFTs. Fig. S9 represents bidirectional transfer plots at $V_{DS} = +100$ V in N_2 atmosphere for transistors constructed of single wire (W/L = 0.048, L = 10.8 μm) and densely packed wire networks (W/L = 2.7, L = 100 μm). The hysteresis of the BPE-PTCDI wire TFTs is relatively small for n-channel OFETs. Fig. S10 exhibits I_{DS} vs. V_G (−20 to +100 V) plots at $V_{DS} = +100$ V measured for 164 cycles in the transistor composed of densely packed wire networks as the active layer. The small variances in the hysteresis and on-to-off current ratio indicate that the wire TFT device is robust in the operation condition.

In ambient atmosphere, the threshold voltage (V_T) and hysteresis of BPE-PTCDI wire transistors increase to some degree, but typically less than a shift of +20 V in V_T, due to the charge trapping by ambient oxidants. A typical bidirectional transfer plot at $V_{DS} = +100$ V under ambient condition for a transistor constructed of densely packed wire networks (W/L = 2.7, L = 100 μm) is illustrated in Fig. S11. The ambient stability could likely be further improved by introducing a high-quality hydroxyl-free dielectric such as a divinyltetramethylsiloxane-bis(benzocyclobutene) derivative (BCB) (1).

Measurements of the Capacitance of SiO_2 Dielectrics. The capacitance of OTS-treated SiO_2 wafer was electrically characterized in sandwich electrode structures with gold pads on the surface of OTS-treated SiO_2 and a highly doped silicon substrate. To minimize the fringe effect of gold pads and obtain more accurate capacitance values, we deposited circular gold pads with 2 different areas (0.0221 and 0.1315 cm^2). Voltage-dependant capacitance measurements were performed by using an Agilent E4980A Precision LCR Meter for frequencies ranging between 20 Hz and 100 KHz. The capacitance vs. frequency for 300-nm-thick SiO_2 treated with OTS is shown in Fig. S12*A*.

The capacitance values measured in gold pads with different sizes are both very close to 10 nF/cm^2 across the overall frequency range. For example, at a frequency of 1 kHz, the capacitance values are 10.32 and 10.30 nF/cm^2 for the electrodes with the area of 0.0221 and 0.1315 cm^2, respectively. Therefore, we used 10 nF/cm^2 for the capacitance of OTS-treated 300-nm-thick SiO_2 dielectric.

We also estimated the capacitance of bare 300-nm-thick SiO_2 dielectrics without OTS treatment (Fig. S12*B*). The capacitance values slightly increase and close to 11 nF/cm^2 throughout the overall frequency range. At a frequency of 1 kHz, the capacitance values are 11.04 and 11.15 nF/cm^2 for the electrodes with the area of 9.817×10^{-3} and 2.212×10^{-3} cm^2, respectively.

In theory, the capacitance can be calculated if the geometry of the electrodes and the dielectric properties of the insulator between the electrodes are known. For example, the capacitance of a parallel-plate capacitor composed of 2 parallel plates of area A separated by a distance d is approximately equal to the following:

$$C = \varepsilon_r \varepsilon_0 \frac{A}{d}, \qquad \textbf{[s1]}$$

where C is the capacitance (F); A is the area of each electrode plate; ε_r is the relative static permittivity (i.e., the dielectric constant) of the material between the electrode plates, (SiO_2 = 3.9); ε_0 is the permittivity of free space where $\varepsilon_0 = 8.854 \times 10^{-12}$ F/m; d is the distance of the plates.

For bare 300-nm-thick SiO_2 dielectric, Eq. **s1** yields ≈11 nF/cm^2, which is in good agreement with the experimentally measured value. The OTS surface-modification layer only slightly decreases the capacitance.

1. Chua L-L, et al. (2005) General observation of n-type field-effect behaviour in organic semiconductors. *Nature* 434:194–199.

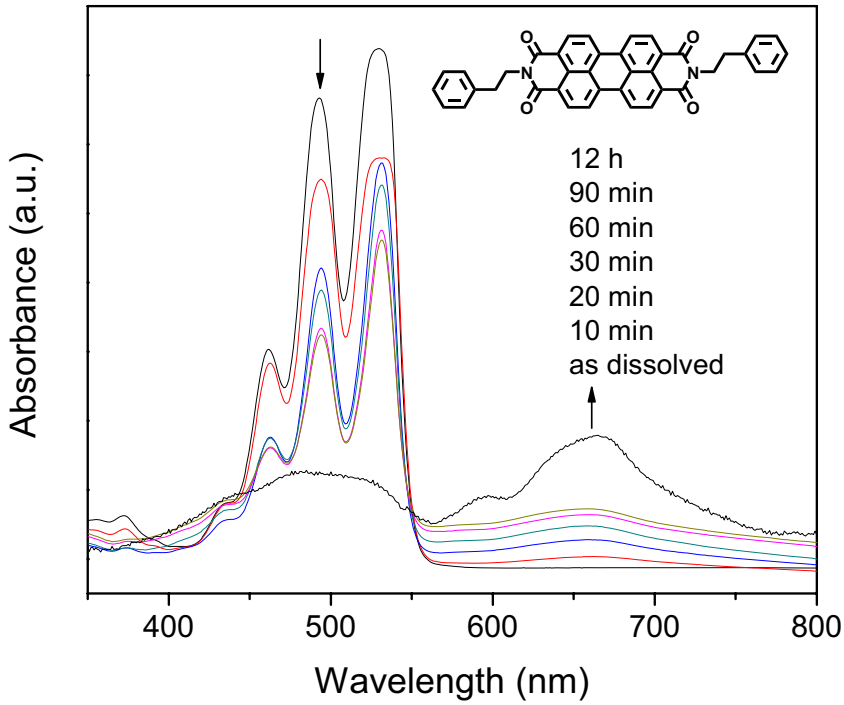

Fig. S1. In situ UV-vis spectra recorded as a function of time from the BPE-PTCDI solution upon cooling from 150 °C. The absorption spectra were recorded at cooling times of 0 (as dissolved), 10, 20, 30, 60, and 90 min and 12 h. *o*-dichlorobenzene was used for the solvent. As the cooling time increased, the absorption bands (0–0, 0–1, 0–2, and 0–3 at 533, 494, 462, and 433 nm) of the molecules decreased gradually, and a new band corresponding to the crystal phase appeared at a longer wavelength (≈665 nm). The isosbestic point at 549 nm indicates a stoichiometric conversion from free molecules to π-stacked crystals.

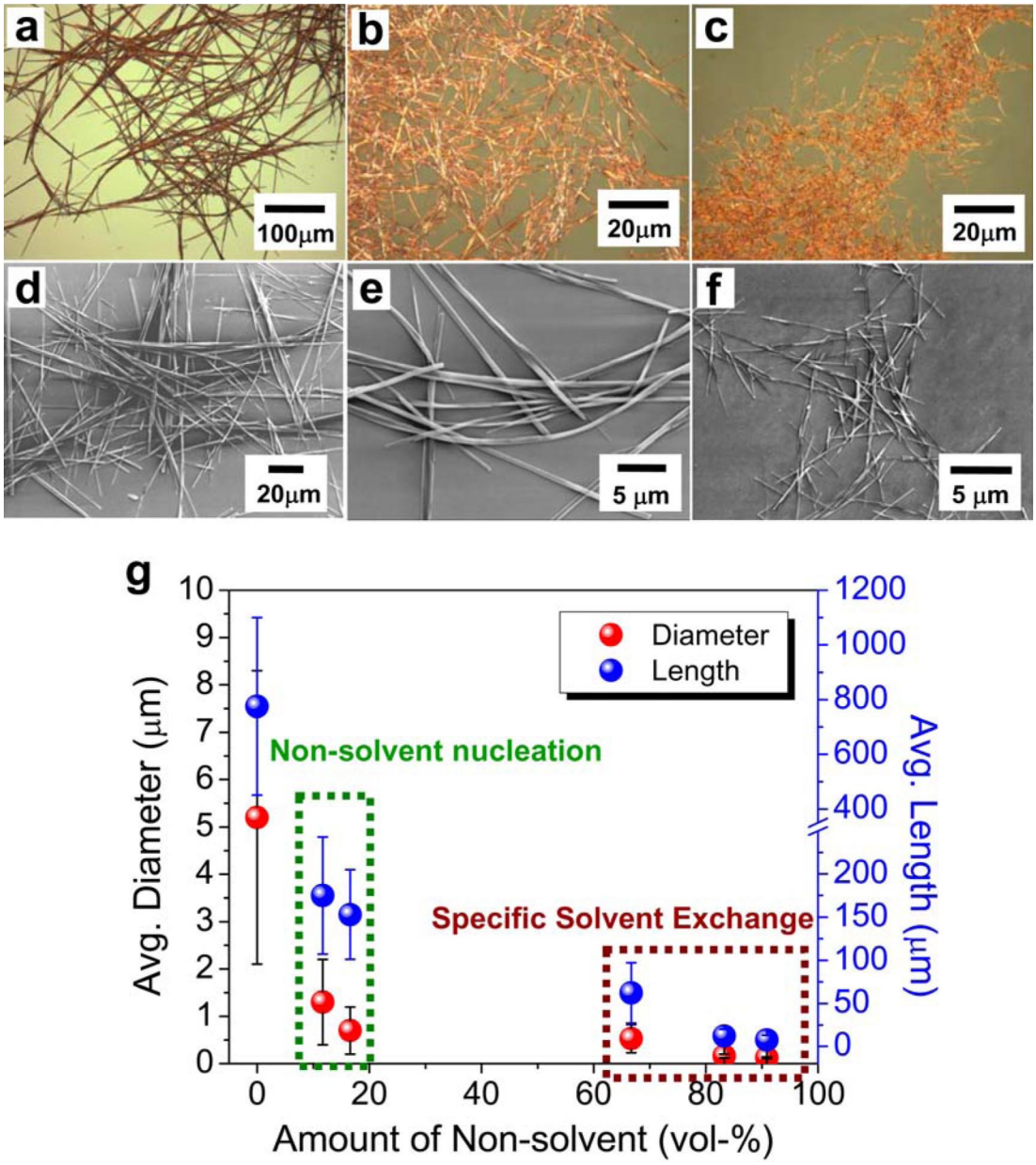

Fig. S2. Characterization of synthesized BPE-PTCDI MWs. (*A*–*C*) Optical images of BPE-PTCDI MWs synthesized by using various amounts of nonsolvent, 11.8 (*A*), 66.7 (*B*), or 90.9 (*C*) vol %. (*D*–*F*) Corresponding SEM images of BPE-PTCDI MWs synthesized by using various amounts of nonsolvent, 11.8 (*D*), 66.7 (*E*), or 90.9 (*F*) vol %. (*G*) Average diameters of BPE-PTCDI MWs as functions of mixing amount of nonsolvent. For these experiments, 18 mg of BPE-PTCDI was dissolved in refluxing *o*-dichlorobenzene (15 mL) in a round-bottom flask with magnetic stirring. In the nonsolvent nucleation, methyl alcohol was added in a fume hood from a dropping funnel after the heating was completely turned off and the flask was removed from the silicon oil bath. Subsequently, the solution was magnetically stirred for 10 s to enhance the mixing of the nonsolvent and obtain wires with more uniform dimensions. In the solvent-exchange method, a small amount of concentrated solution (1.2 mg BPE-PTCDI in 1 mL of *o*-dichlorobenzene) was added into an excess of methyl alcohol and then magnetically stirred for 10 s. For the details for the collections of resulting NW/MWs, see *Methods*.

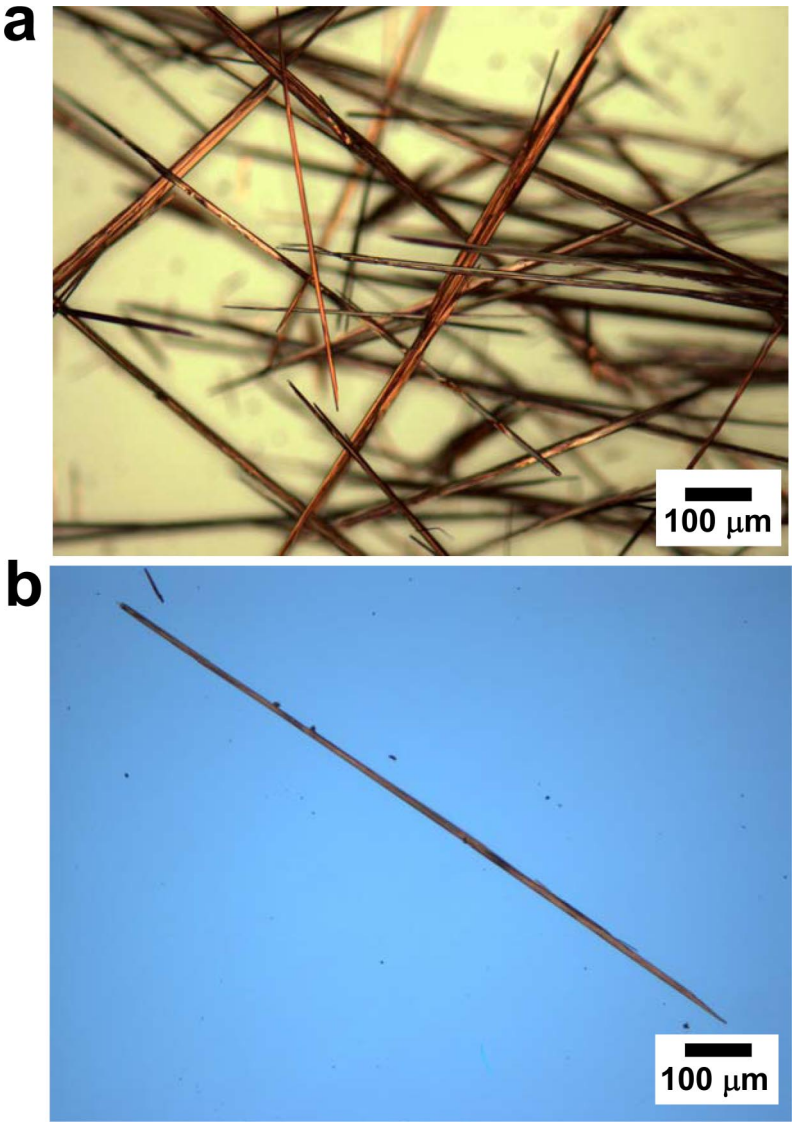

Fig. S3. Millimeter-length BPE-PTCDI MWs. Bright-field optical images of millimeter length BPE-PTCDI MWs (*A*) and a single BPE-PTCDI MW (*B*). The heated solution containing BPE-PTCDI molecules was cooled from ≈150 °C to room temperature very slowly over >12 h to increase the MW length.

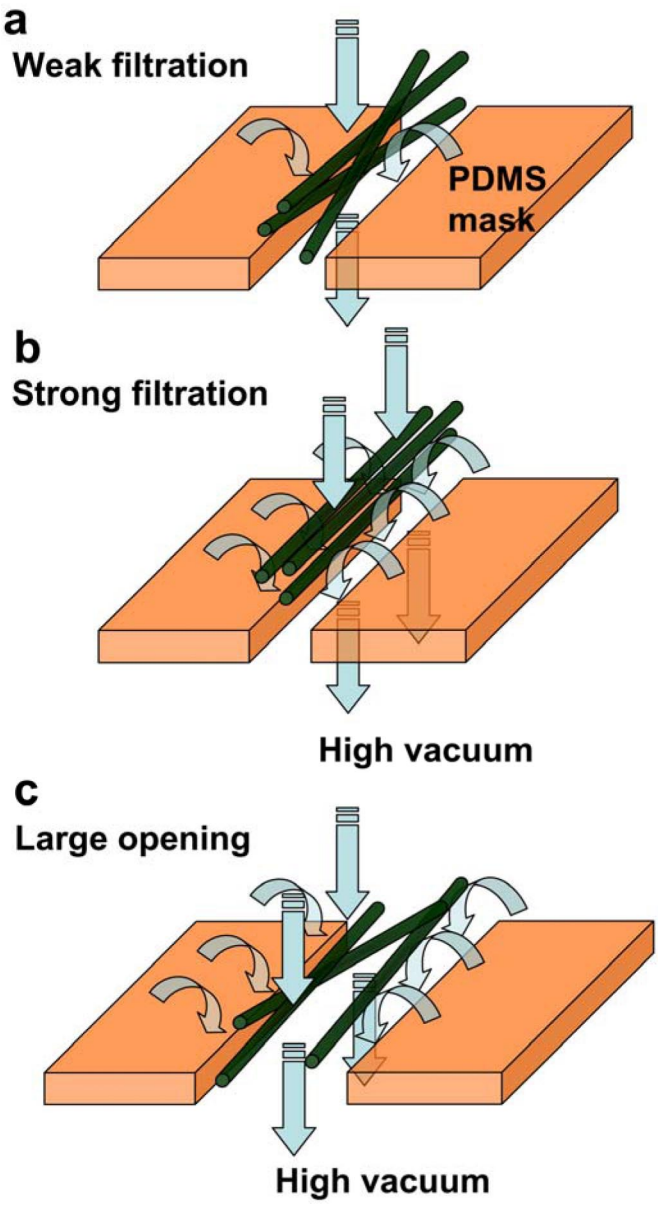

Fig. S4. Schematic diagram of MW alignment by the filtration-and-transfer (FAT) method. (*A*) Weak filtration. Low suction cannot provide sufficient lateral flow, which acts as torque to orient MWs parallel to the long axis of the opening. (*B*) Strong filtration. High suction orients MWs along the longitudinal direction of the pattern by causing a lateral flow strong enough to rotate MWs along the long axis of the pattern. (*C*) Wide pattern width with regard to the MW length. The wide pattern width causes the weakening of the torque, making the MW alignment relatively worse.

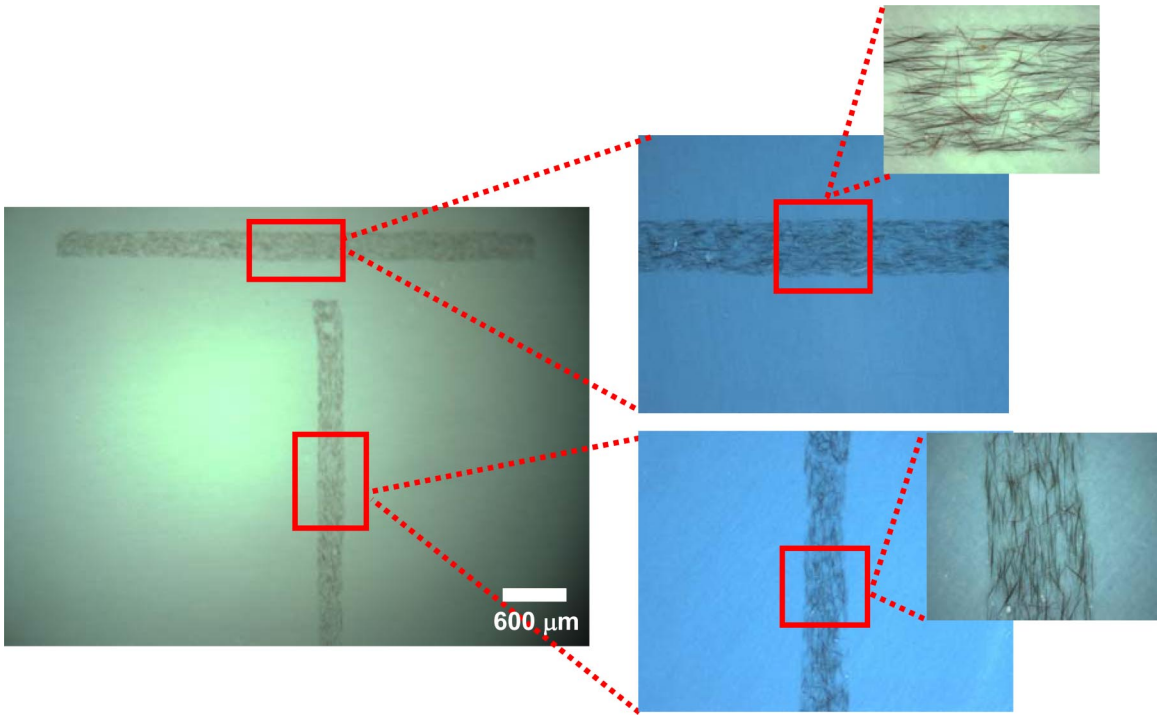

Fig. S5. ''T-shaped'' pattern. Multiple MW patterns aligned in different directions on the same substrate are obtained in one filtration step. Patterning experiments using ''T-shaped'' mask allow for perpendicularly aligned, discrete MW patterns on the same substrate at once. This kind of alignment is difficult to achieve with other fluidic flow methods.

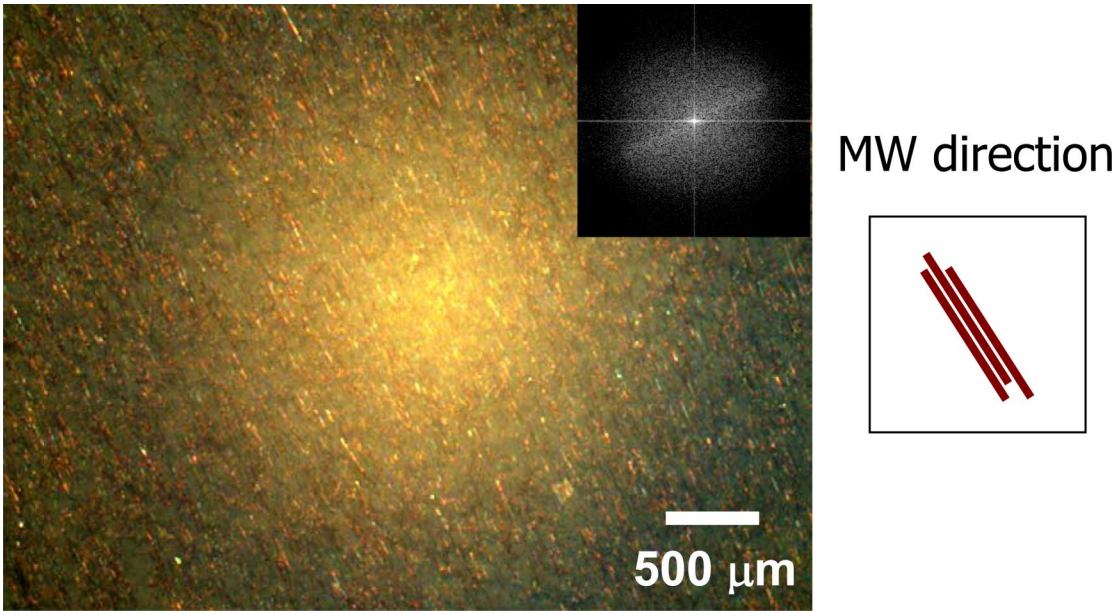

Fig. S6. Large area alignment of BPE-PTCDI MWs. A bright-field optical image of aligned BPE-PTCDI MWs over a large area. The *Inset* is the Fourier transform of the image indicating alignment of the microwires perpendicular to the faint band stretching from the first to the third quadrant. Organic MWs could be aligned over nearly the entire area of an AAO membrane with 2.5-cm diameter, with pattern dimensions of several millimeters × centimeter scale. The pressure drop across the filter stack can be increased by pressing the MW dispersion with a syringe.

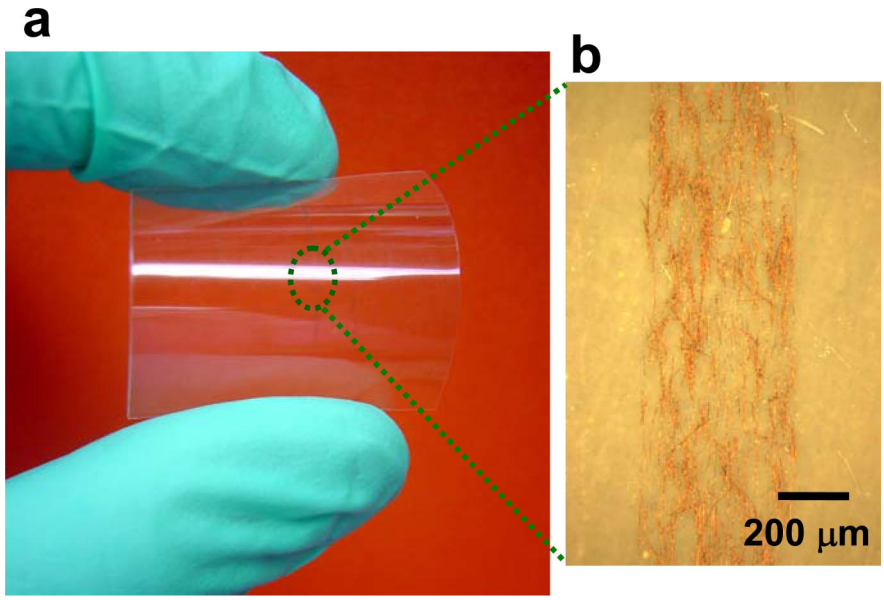

Fig. S7. Transfer of organic MW patterns onto a flexible plastic substrate. (*A*) A photograph of BPE-PTCDI MW patterns transferred onto a polyethylene terephthalate (PET) film. (*B*) A bright-field optical image of a BPE-PTCDI MW pattern transferred onto the PET film.

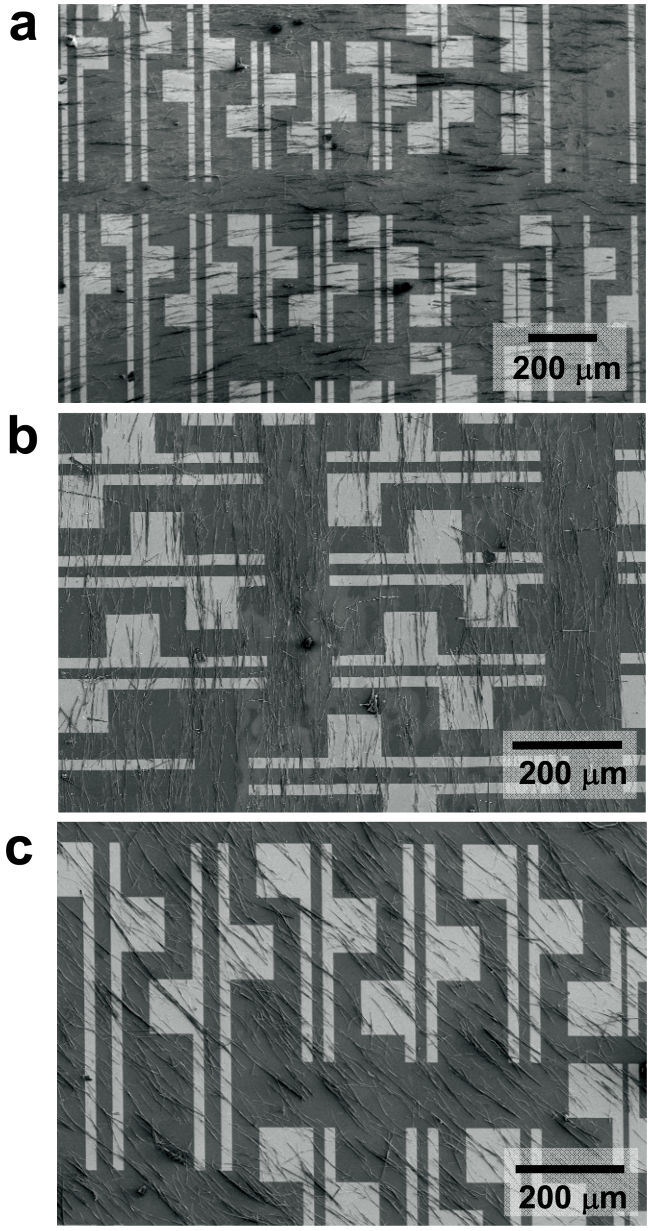

Fig. S8. SEM images of BPE-PTCDI MWs transferred onto bottom-contact SiO_2/Si substrates by FAT method. (*A* and *B*) MW alignment parallel to channel length. (*C*) MW alignment with slant directions with regard to channel length. Aligned MWs can be transferred easily onto OTS-treated SiO_2 substrates. The direction of MW alignment with regard to channel length can be controlled readily by tuning the channel direction on the electrode substrate to the MW alignment direction on the filter upon stacking.

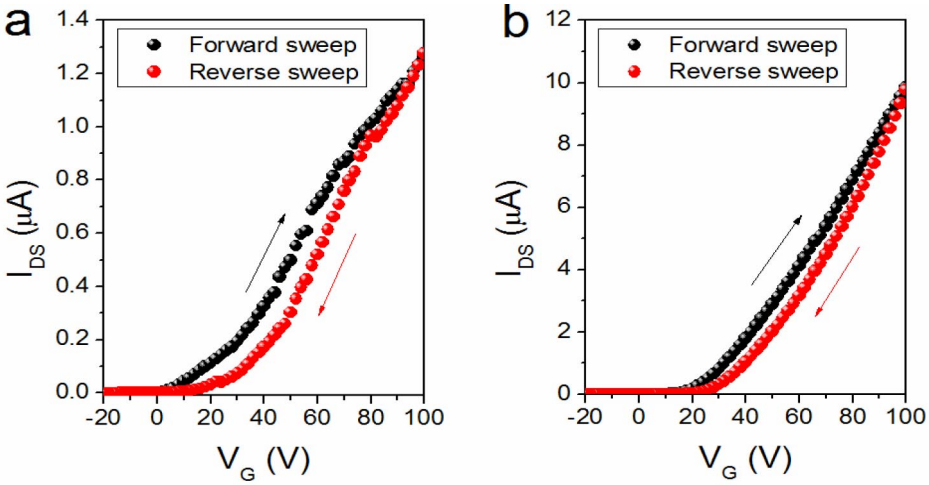

Fig. S9. Bidirectional transfer plots at $V_{DS} = +100$ V in N_2 atmosphere for transistors constructed of a single wire (W/L = 0.048, L = 10.8 μm) (*A*) and densely packed wire networks (W/L = 2.7, L = 100 μm) (*B*).

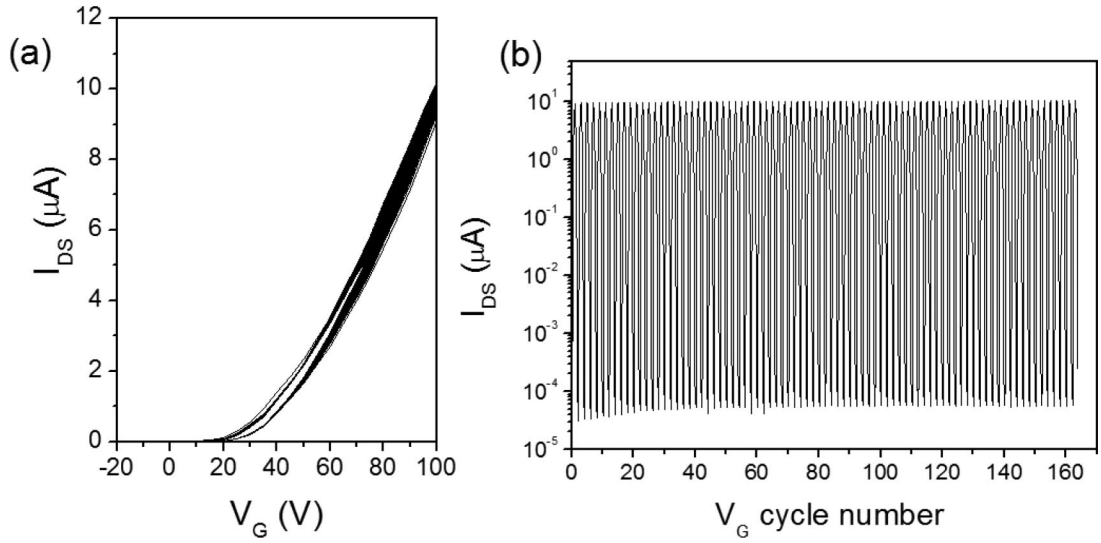

Fig. S10. I_{DS} vs. V_G (−20 to +100 V) plots at V_{DS} = +100 V measured for 164 cycles for transistors composed of densely packed wire networks (W/L = 2.7, L = 100 μm) as the active layer. (*A*) Transfer characteristics recorded sequentially. (*B*) Log-scale plot of I_{DS} as functions of V_G cycles.

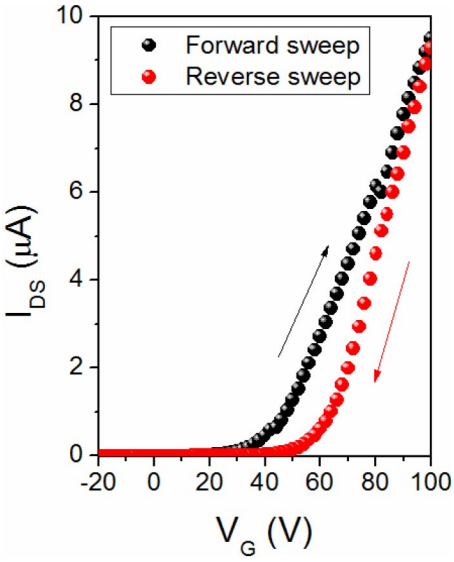

Fig. S11. Bidirectional transfer plots at $V_{DS} = +100$ V in ambient air (relative humidity ≈38%) for a transistor constructed of densely packed wire networks (W/L = 2.7, L = 100 μm) as the active layer.

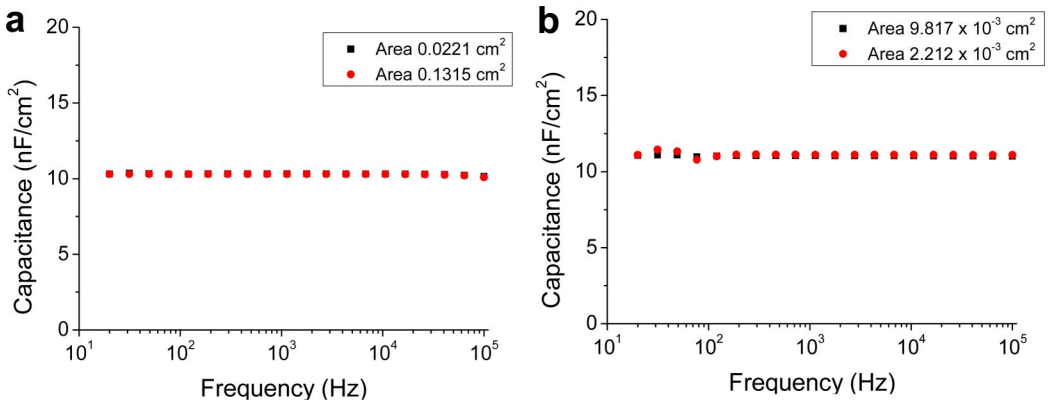

Fig. S12. Capacitance vs. frequency for (a) OTS-treated 300-nm-thick SiO_2 (*A*)and bare 300-nm-thick SiO_2 (*B*). The electrode pad areas are shown in the legends.

Table S1. A summary of HOMO and LUMO levels of BPE-PTCDI in solution state, vacuum-deposited thin film, and microwire form

State	HOMO (eV)	LUMO (eV)	E_g (eV)
Solution[a]	−6.10	−4.10	2.00
Thin film[b]	−6.07[c]	−4.26	1.81[d]
Microwire	−6.04[c]	−4.39	1.65[d]

The LUMO levels become lower as the levels of structural perfection increase, because of the enhanced electronic coupling between molecules in crystalline solids (1).

[a]Literature values (2, 3) measured by cyclic voltammetry.

[b]the 45-nm thin film made by evaporation under high vacuum ($\approx 10^{-6}$ torr) at a deposition temperature of 125 °C.

[c]Work function measured in ambient air by ultraviolet photoelectron spectroscopy (UPS).

[d]E_g, the band gap, the long wavelength absorption edge on the UV-vis spectra.

1. Brédas J-L, Beljonne D, Coropceanu V, Cornil J (2004) Charge-transfer and energy-transfer processes in π -conjugated oligomers and polymers: A molecular picture. *Chem Rev* 104:4971–5003
2. Ling M-M, et al. (2007) Air-stable n-channel organic semiconductors based on perylene diimide derivatives without strong electron withdrawing groups. *Adv Mater* 19:1123–1127.
3. Liu A, et al. (2008) Control of electric field strength and orientation at the donor–acceptor interface in organic solar cells. *Adv Mater* 20:1065–1070.